Tube-in-Tube Structure Design and *In-situ* Growth of Fe₃C for Efficient Reaction Kinetics in Lithium-Sulfur Batteries

Miao Sun+,[a] Jin Luo+,[a] Shuang Wang,[a] Yinhua Wang,[a] Haijun Zhang,*[a] and Wen Lei*[a]

To improve the sulfur reaction kinetics and inhibit the notorious shuttle effects, a tube-in-tube structure decorated by carbon nanotubes (CNT) and Fe₃C nanoparticles (TIT/Fe₃C-CNT) is designed as sulfur host for lithium-sulfur batteries (LSBs) in this work. The construction of tube-in-tube structure increases the active sites and the specific surface area of the material. Additionally, Fe₃C nanoparticles can effectively adsorb the soluble lithium polysulfides and promote their catalytic conversion, thus greatly alleviating the shuttle effects. As a result of these advantages, the TIT/Fe₃C-CNT-based cathode exhibits a high reversible capacity of 841 mAh g^{-1} after 200 cycles with a low decay of 0.056% per cycle at 0.5 C. This work provides a promising and reasonable approach to the rational design of sulfur host for LSBs.

Introduction

Long-cycle and high-energy-density batteries have been extensively developed and are becoming increasingly important components of the global energy storage system as the energy demand continues to rise.[1–4] Among these, lithium-sulfur batteries are gaining more and more attention as a promising energy storage technology.[5,6] When combined with a lithium metal anode, the high theoretical specific capacity of sulfur (1673 mAh g^{-1}) may raise the theoretical energy density of the battery to 2600 Wh kg^{-1},[7–9] which is more than three times greater than contemporary lithium-ion batteries.[10] Additionally, sulfur-positive electrodes have the benefit of being widely available and eco-friendly.[11] Thus, studies on lithium-sulfur batteries can contribute to the development of affordable, environmentally friendly, high energy density, and sustainable energy storage technologies.[12] However, there are several serious issues with lithium-sulfur batteries that restrict their commercial use: 1) the insulative nature of elemental sulfur and its reaction products may lead to reduced utilization of the active material;[13,14] 2) the highly soluble long-chain lithium polysulfide intermediates in the electrolyte facilitate their migration to the anode and subsequent interaction with metallic lithium. In addition to causing the loss of the active material, this shuttle effect also severely corrodes the lithium anode and consumes the electrolyte. Consequently, this leads to low coulombic efficiency and poor cycling life;[15,16] 3) sulfur undergoes significant volume changes during the lithiation process, resulting in electrode fragmentation and subpar cyclic performance.[17]

The most common approach to address these issues is to combine a conductive porous host material with sulfur to form composite materials, with porous carbon materials being a common choice.[18–20] One-dimensional (1D) carbon materials outperform other carbon materials in terms of long-range conductivity and mechanical properties, which improve electrode stability.[21,22] They also offer ample space and efficient physical adsorption for sulfur particles and polysulfides. Abdul Razzaq[23] used carbon nanotubes (CNT) to construct a sulfur carrier, and the results showed that the carbon nanotubes improved the material porosity and provided a conductive pathway. Finally, the assembled lithium-sulfur battery delivered a high initial discharge capacity of 1610 mAh g^{-1} at 0.2 C. Li[24] designed a sulfur host consisting of carbon nanofibers (CNF) to improve the conductivity of sulfur and the results showed that the composite cathode of sulfur and carbon nanofibers maintained a high capacity of 672 mAh g^{-1} after 1000 cycles. Unfortunately, the short-term suppression of polysulfide diffusion is limited by the weak contact between sulfur and carbon. More significantly, the restricted internal area of 1D carbon materials always makes it difficult to load large amounts of sulfur particles.[25] To address these issues, structural modifications can be made to 1D hollow materials,[26] and metal compounds containing catalytic elements can be introduced to create sulfur host carriers.[27] These modifications aim to increase sulfur loading, enhance lithium polysulfide chemisorption, and improve conversion kinetics.

Here, we constructed a sulfur host for lithium-sulfur batteries using carbon fiber with a tube-in-tube structure modified by the catalytic component Fe₃C. In addition to providing sufficient space for sulfur loading, the hollow carbon fiber material, with its tubular casing construction, can effectively mitigate the volume expansion of sulfur species that occurs during the charging and discharging process. Moreover, the CNT synthesized within the hollow carbon fibers establishes a three-dimensional conductive network, thereby augmenting internal electrical conductivity and facilitating electron transfer. Furthermore, the Fe₃C nanoparticles inserted both within and outside the hollow carbon fibers' shell layer can lessen the

[a] M. Sun,+ J. Luo,+ S. Wang, Y. Wang, H. Zhang, Dr. W. Lei
The State Key Laboratory of Refractories and Metallurgy
Wuhan University of Science and Technology
Wuhan, Hubei 430081, P. R. China
E-mail: zhanghaijun@wust.edu.cn
leiwen@wust.edu.cn
[+] These authors contributed equally to this work
📖 Supporting information for this article is available on the WWW under
https://doi.org/10.1002/batt.202400224

Batteries & Supercaps

Research Article
doi.org/10.1002/batt.202400224

Chemistry
Europe

European Chemical
Societies Publishing

shuttle effect, accelerate the chemical adsorption of lithium polysulfide, and enhance the battery's redox kinetics.

Results and Discussion

The synthesis procedure of TIT/Fe$_3$C-CNT is illustrated in Figure 1a. We prepared polyvinylpyrrolidone@polystyrene (PVP@PS) and PS fibers through coaxial electrospinning. As depicted in Figure S1(a) and (b), both PVP@PS and PS fibers displayed smooth surfaces and consistent dimensions, with an average diameter of around 1.5 μm. Then, the PVP component within the PVP@PS fibers was completely removed by thorough washing with a large volume of water to yield hollow PS (HPS) fibers. Figure 1a illustrated that the diameter of the HPS fibers remained largely unchanged, with an inner diameter of approximately 1 μm. Following this, for the *in-situ* coating of polypyrrole (PPy), the PS and HPS fibers were immersed in a pyrrole aqueous solution for polymerization. Figures 1b–c demonstrated that both PS and HPS fibers exhibited a rougher texture and a slight increase in diameter after being coated with PPy, indicating successful encapsulation.

We employed FTIR spectroscopy to qualitatively analyze the structural properties of the fabricated PVP@PS, PS, HPS, PS@PPy, and HPS@PPy fibers to ascertain the effective coating of PPy. The FTIR curve of PVP@PS fibers, as depicted in Figure 1d, revealed absorption peaks at 1290 cm^{-1} (PVP's C—N stretching

vibration peak) and 1650 cm^{-1} (PVP's C=O bending vibration peak).[28] Furthermore, the observed peaks at 696 cm^{-1}, 755 cm^{-1}, and 1030 cm^{-1} represent characteristic vibrational modes of monosubstituted benzene rings. Similarly, the absorption peaks detected at 1452 cm^{-1}, 1490 cm^{-1}, and 1600 cm^{-1} correspond to the stretching vibrations of the benzene rings, which are distinctive features of PS.[29] Following the effective removal of PVP, the HPS fibers demonstrated an absence of absorption peaks at 1290 and 1650 cm^{-1}, distinguishing them from the PVP@PS fibers. The FTIR spectrum of PS@PPy and HPS@PPy fibers showed three distinct absorption peaks of PPy: the stretching vibration peak of the C—H bond at 970 cm^{-1}, the stretching vibration peak of the N—H bond at 1040 cm^{-1}, and the skeletal ring stretching and shrinking vibration peak at 1540 cm^{-1}.[30] The products of PS@PPy and HPS@PPy fibers after high-temperature treatment were named HCF, and TIT respectively. Following carbonization and chemical vapor deposition treatment, the FeCl$_3$-containing HPS@PPy-FeCl$_3$ fibers were put in a tube furnace with dicyandiamide to produce TIT/Fe$_3$C-CNT (see Experimental Section).

To examine the physical structure of the materials, we analyzed the carbonized products HCF, TIT, and TIT/Fe$_3$C-CNT using XRD (X-ray diffraction). As shown in Figure 1e. TIT and HCF exhibited broad diffraction peaks at around 24°, corresponding to the (002) crystal plane of graphite. In addition, the diffraction peaks of TIT/Fe$_3$C-CNT were sharper due to the presence of Fe$_3$C, which facilitated the *in-situ* catalytic generation of CNT on the surface and inside the hollow fibers during the chemical vapor deposition process.[31] The diffraction peaks of TIT/Fe$_3$C-CNT at 37.7°, 42.9°, 43.7°, 44.6°, 45.9°, 49.1°, and 54.4° could be assigned to Fe$_3$C peaks (JCDPS, No.34-0001), confirming the conversion of FeCl$_3$ in the raw material to Fe$_3$C.[32]

The surface morphologies of the carbonized HCF, TIT, and TIT/Fe$_3$C-CNT were analyzed by SEM. As shown in Figure 2, during the carbonization process of PS@PPy and HPS@PPy, PS and HPS decomposed to form voids at high temperatures. And the PPy on the outer surface formed a carbon shell after carbonization, leading to the formation of HCF (Figure 2a) and TIT (Figure 2b), respectively. Moreover, HPS@PPy-FeCl$_3$ also formed a tube-in-tube structure under high-temperature conditions, and FeCl$_3$ generated Fe$_3$C *in situ*. With increasing temperature, Fe$_3$C on the surface of TIT/Fe$_3$C-CNT acted as an *in-situ* catalyst for generating a large number of CNT (Figure 2c). The 3D network formed by these CNT not only interconnected the carbon fibers but also improved the conductivity and shortened the electron transfer path, ensuring the enhanced electrochemical performance of lithium-sulfur batteries.

Further analysis of the internal structures of HCF, TIT, and TIT/Fe$_3$C-CNT was conducted using TEM. Figure 2d showed the TEM image of carbonized HCF. PS decomposes into a hollow structure after heat treatment. Figure 2e presented the TEM image of carbonized TIT, indicating that the HPS fibers also decomposed after heat treatment. Due to the uniform coating of PPy on both the inner and outer sides of HPS, a tube-in-tube structure of carbon fibers was formed after carbonization, as indicated by orange dashed lines in Figure 2e.
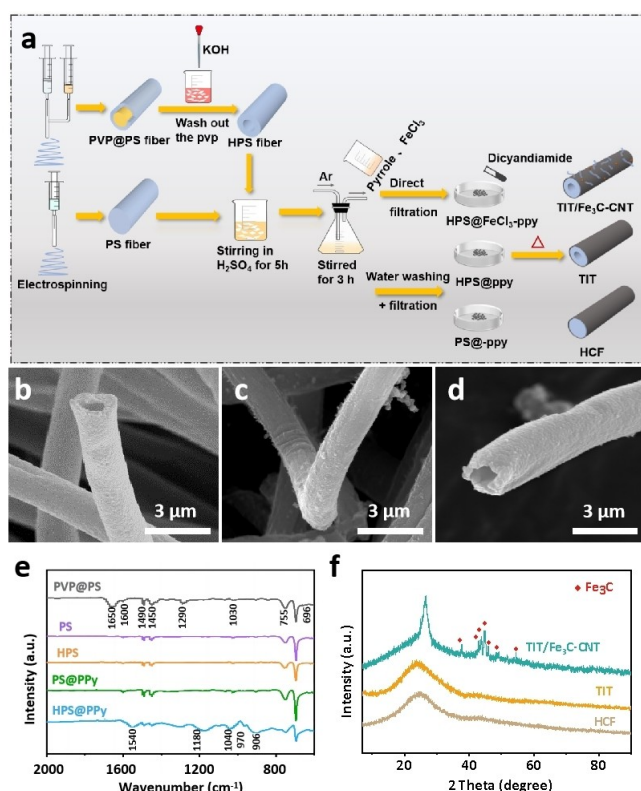

Figure 1. (a) Schematic illustration of the preparation process of HPS, TIT, TIT/Fe$_3$C-CNT. (b–d) SEM images of HPS, PS@PPy and HPS@PPy. (e) FTIR spectra of PVP@PS, HPS, PS, PS@PPy, and HPS@PPy. (f) XRD patterns of HCF, TIT, and TIT/Fe$_3$C-CNT.
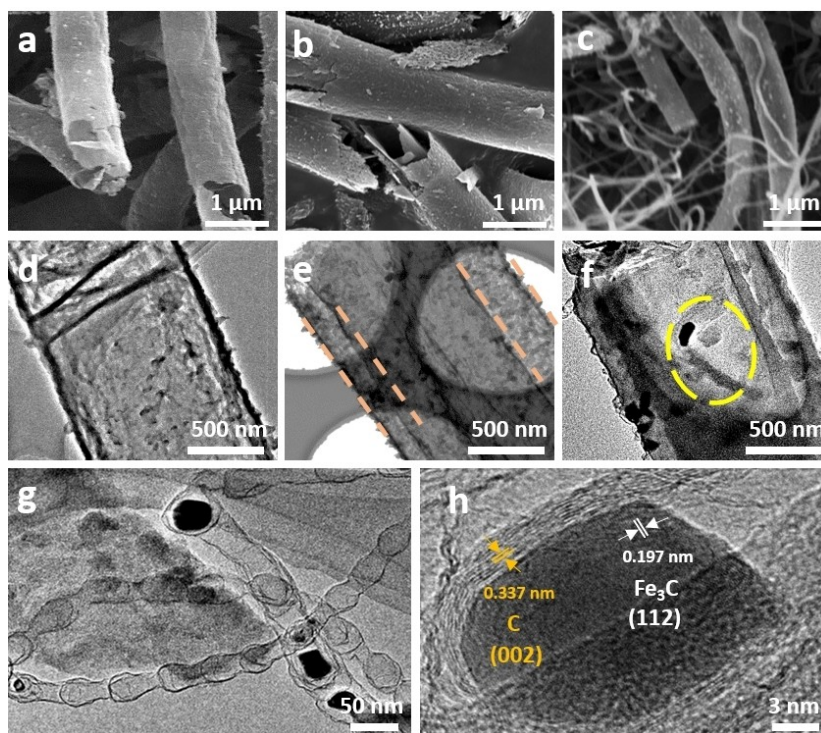
Figure 2. (a–c) SEM images of HCF, TIT and TIT/Fe$_3$C-CNT. (d–f) TEM images of HCF, TIT, and TIT/Fe$_3$C-CNT. (g, h) SEM and HRTEM images of Fe$_3$C-CNT.

The TEM image of TIT/Fe$_3$C-CNT shown in Figure 2f revealed a tube-in-tube structure similar to TIT after undergoing carbonization. During the heat treatment, FeCl$_3$ reacted with the decomposed dicyandiamide to produce Fe$_3$C particles. Fe$_3$C particles catalyze the in-situ formation of CNT from the decomposition of dicyandiamide on the surface and inside the TIT, as indicated by the yellow ellipsoids in Figure 2f. Specially, FeCl$_3$ in the raw material forms Fe$_3$C nanoparticles directly on both the inner and outer surface of TIT, providing the primary location for CNT growth. The introduction of dicyandiamide acts as the catalyst precursor for CNT preparation, with carbon beginning to diffuse as the temperature rises.[33] Consequently, CNT are synthesized in situ within and on the surface of TIT, facilitated by Fe$_3$C nanoparticles as catalysts. These *in situ* formed Fe$_3$C particles and CNT were expected to adsorb long-chain lithium polysulfides dissolved in the electrolyte and accelerate their catalytic conversion. Additionally, they could enhance the conductivity of the electrode and effectively improve the rate performance of the battery.

To further investigate the microstructure of materials, we analyzed Fe$_3$C-CNT using TEM and HRTEM. As shown in Figure 2g, Fe$_3$C particles were encapsulated within CNT, and the formed CNT exhibited a bamboo-like morphology, indicating that CNT were catalytically grown by Fe$_3$C particles. The results from HRTEM (Figure 2h) showed that Fe$_3$C particles were surrounded by multi-layered graphitic carbon, suggesting that Fe$_3$C promotes the graphitization of carbon during high-temperature treatment.[34] Further analysis of the lattice fringes of the two materials revealed interplanar spacings of 0.377 nm

and 0.197 nm, corresponding to the (002) crystal plane of graphite[35] and the (112) crystal plane of Fe$_3$C,[36] respectively.

The elemental composition and distribution of the materials were studied using EDS mapping. Figure S2 showed the TEM image and element distribution map of HCF. It is evident from the figure that the elements C, N, and O were uniformly distributed on the surface of the material. Figures S3 and S4 showed the TEM images and element distribution maps of TIT and Fe$_3$C/CNT, respectively. From these images, it could be observed that the elements C, N, and O were also uniformly distributed on the surface of TIT (Figure S3). In the element distribution map of Fe$_3$C/CNT (Figure S4), it could be observed that the Fe element was uniformly distributed on the surface of the particles, which aligned with the HRTEM test result of Fe$_3$C shown in Figure 2h.

We analyzed the structures of HCF, TIT, and TIT/Fe$_3$C-CNT using Raman spectroscopy. As shown in Figure S5. The curves of the three materials exhibited two distinct peaks at 1379 and 1580 cm^{-1}, corresponding to the D band and G band, respectively. The calculated I$_D$/I$_G$ ratios for HCF, TIT, and TIT/Fe$_3$C-CNT are 1.08, 1.07, and 1.01, respectively. The higher I$_D$/I$_G$ values for TIT and HCF samples were attributed to the presence of more defects in nitrogen-doped carbon fibers. The lower I$_D$/I$_G$ value for the TIT/Fe$_3$C-CNT sample could be attributed to the catalytic carbonization and growth of CNT facilitated by Fe$_3$C.[37,38] The results of the Raman spectroscopy were consistent with the XRD test results (Figure 1e). To investigate the surface chemical structure and elemental composition of materials, we analyzed HCF, TIT, and TIT/Fe$_3$C-CNT using XPS. As shown in Figure S6, HCF, TIT, and TIT/Fe$_3$C-CNT all contain C, N,

Batteries & Supercaps

Research Article
doi.org/10.1002/batt.202400224

Chemistry Europe
European Chemical
Societies Publishing

and O elements. Additionally, TIT/Fe$_3$C-CNT also contained Fe elements, which was consistent with the EDS test results (Figure S4).

Figures 3(a–c) showed the N 1s spectra of HCF, TIT, and TIT/Fe$_3$C-CNT, respectively. The peaks in the N 1s spectra could be fitted to four components: 397.5, 399, 399.8, and 402.8 eV, corresponding to pyridinic N, pyrrolic N, graphitic N, and oxidized N respectively. We conducted thermogravimetric spectral analysis on HCF, TIT, and TIT/Fe$_3$C-CNT (Figure S9). The samples were blended with sublimed sulfur at a ratio of 3:7 by weight and heated to 155 °C for 12 h to melt the sulfur for it to infiltrate the hosts' pores. Upon calculation, the residual weight with the three materials, HCF/S, TIT/S, and TIT/Fe$_3$C-CNT/S, was determined to be 20 wt%, 35.6 wt%, and 45.1 wt%, respectively. XRD characterization was performed on HCF/S, TIT/S, and TIT/Fe$_3$C-CNT/S samples after the sulfur loading, as shown in Figure 3d. Compared to the XRD patterns before the sulfur loading, almost all diffraction peaks corresponded to the characteristic peaks of sulfur (JCPDS. No.78-1888).

The wettability of HCF, TIT, and TIT/Fe$_3$C-CNT samples with electrolytes was tested separately. As shown in Figure S5, after adding the electrolyte, obvious droplets could still be observed on the surface of HCF even after 0.8 seconds. In contrast, for the TIT sample, almost no droplets could be observed during the same period, indicating that TIT was conducive to electrolyte infiltration due to its structure. In addition, when an equal amount of electrolyte was dropped onto the surface of TIT/Fe$_3$C-CNT, the sample completely absorbed the electrolyte after 0.4 seconds, indicating that the TIT/Fe$_3$C-CNT sample had better electrolyte wetting ability compared to the HCF and TIT specimens. The excellent wettability of TIT/Fe$_3$C-CNT could be attributed to the structure of TIT and the three-dimensional network structure constructed by CNT, which promoted sufficient contact between the electrolyte and the sample, accelerating the absorption of the electrolyte by the latter.

To further test the specific surface area of the samples, the N$_2$ adsorption-desorption isotherm method was used to charac-terize HCF, TIT, and TIT/Fe$_3$C-CNT. As shown in Figure S6(a–c), the calculated specific surface area of TIT/Fe$_3$C-CNT was 301.32 m^2 g^{-1}, significantly much higher than the surface areas of HCF and TIT (30.26 and 70.84 m^2 g^{-1}, respectively). The reason for the huge difference in specific surface area may be that during the chemical vapor deposition process of TIT/Fe$_3$C-CNT, FeCl$_3$ in-situ transformed to Fe$_3$C, leading to the creation of numerous micropores. Secondly, CNT in-situ catalyzed by Fe$_3$C also increased the specific surface area of the sample to some extent. In addition, due to the tube-in-tube structure of TIT, its specific surface area was also larger than that of HCF. An increase in specific surface area was beneficial for reducing electrode quality and ultimately improving the mass energy density of lithium-sulfur batteries.

A series of electrochemical tests were performed on HCF, TIT, and TIT/Fe$_3$C-CNT specimens to investigate the electrochemical performance of the assembled lithium-sulfur batteries. Figure 4a showed the cyclic voltammetry (CV) curves of the three specimens assembled into cells at a scanning rate of 0.1 mV/s, which exhibited typical lithium-sulfur battery CV curves.[39] Further analysis of the CV curves of the three specimens revealed that TIT/Fe$_3$C-CNT had a higher reduction potential and lower oxidation potential compared to HCF and TIT. Therefore, TIT/Fe$_3$C-CNT had a smaller potential difference between oxidation and reduction, indicating that HCF and TIT experienced more pronounced electrode polarization. This was because the polar Fe$_3$C could effectively adsorb long-chain lithium polysulfides dissolved in the electrolyte during the mutual transformation process between soluble lithium polysulfides and insoluble lithium polysulfides, and promoting the rapid ion transport of lithium polysulfides on their surface, thereby mitigating the shuttle effect. Compared with HCF and TIT, TIT/Fe$_3$C-CNT also exhibited sharper oxidation-reduction peaks, further indicating that the introduction of Fe$_3$C accelerated the catalytic conversion of lithium polysulfides. In addition, TIT exhibited less electrochemical polarization and sharper peaks than HCF. This was attributed to the unique structure of TIT, which endowed it with a high conductivity. This structure guaranteed the conversion of lithium polysulfides and, to some extent, enhanced the electrochemical performance of the battery.

In order to further evaluate the electrochemical performance of HCF, TIT, and TIT/Fe$_3$C-CNT, we performed electrochemical impedance spectroscopy (EIS) on each of the three samples. As shown in Figure 4b, the impedance diagrams of each sample consist of a semicircle in the high frequency region and a slash line in the low frequency region, corresponding to the charge transfer resistance and the ion diffusion resistance, respectively. It can be seen that TIT/Fe$_3$C-CNT has not only a smaller charge transfer resistance (R$_{ct}$) but also a faster charge transport rate. Firstly, the presence of CNT contributed to the creation of a richer conductive network to produce faster charge transfer rates in charge and discharge. Secondly, Fe$_3$C nanoparticles facilitate mass transfer on the surface of the electrode material when promoting the conversion of polysulfides.
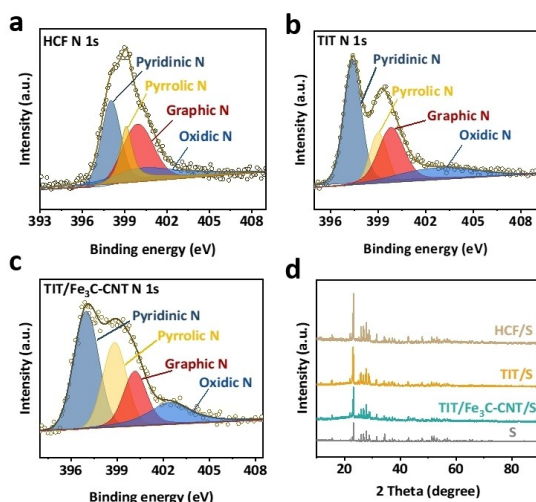
Figure 3. High-resolution N 1s mapping of HCF (a), TIT (b), and TIT/Fe$_3$C-CNT (c). (d) XRD pattern of HCF/S, TIT/S and TIT/Fe$_3$C-CNT/S.
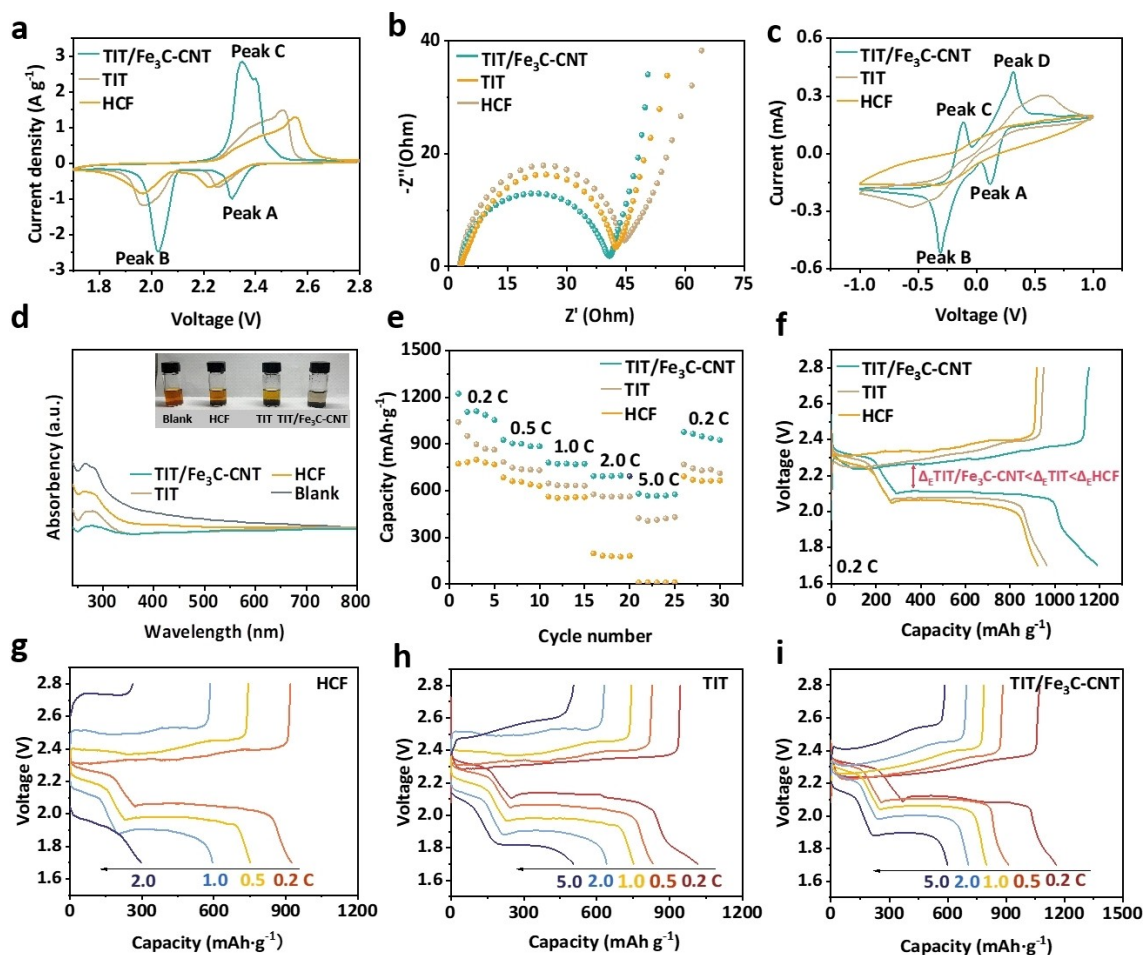
Batteries & Supercaps

Research Article
doi.org/10.1002/batt.202400224

Chemistry
Europe
European Chemical
Societies Publishing

Figure 4. (a) CV curves of HCF, TIT, and TIT/Fe$_3$C-CNT at a scan rate of 0.1 mV/s. (b) EIS spectra of HCF, TIT, and TIT/Fe$_3$C-CNT. (c) CV curves of symmetrical cells under the scan rate of 1 mV/s for HCF, TIT and TIT/Fe$_3$C-CNT. (d) UV-vis spectra and optical images (inset) of HCF, TIT, and TIT/Fe$_3$C-CNT with Li$_2$S$_6$ solution. (e) Rate performance of HCF, TIT, and TIT/Fe$_3$C-CNT. (f) Charge/discharge curves of HCF, TIT, and TIT/Fe$_3$C-CNT at 0.2 C.(g–i) Charge/discharge curves of HCF, TIT and TIT/Fe$_3$C-CNT at different rates, respectively.

The assembled symmetric cells of HCF, TIT, and TIT/Fe$_3$C-CNT were then tested, as shown in Figure 4c. TIT/Fe$_3$C-CNT exhibited four peaks (two reduction peaks and two oxidation peaks) during the conversion of lithium polysulfides. While the peak positions of the oxidation/reduction peaks of TIT were not as distinct as those of TIT/Fe$_3$C-CNT, indicating that the presence of Fe$_3$C particles could accelerate the redox kinetics of lithium polysulfides. In addition, HCF showed almost no significant peaks, further demonstrating the favorable effect of TIT on the conversion of lithium polysulfides. HCF and TIT showed significant hysteresis potential compared to TIT/Fe$_3$C-CNT. This was due to the low catalytic activity of HCF and TIT towards lithium polysulfides, which hindered the rapid reduction of a substantial quantity of lithium polysulfides. Consequently, this led to electrode polarization and potential hysteresis. Li$_2$S$_6$ adsorption experiments were conducted separately on HCF, TIT, and TIT/Fe$_3$C-CNT, as shown in Figure 4d. After being left undisturbed for 12 hours, the supernatant of TIT/Fe$_3$C-CNT became clear, indicating complete adsorption of Li$_2$S$_6$. While the supernatants of TIT and HCF became lighter in color, indicating weaker adsorption of Li$_2$S$_6$ by the nitrogen-

doped carbon materials. The UV-visible absorption spectroscopy (UV-vis) results further demonstrated the excellent adsorption capacity of Fe$_3$C for lithium polysulfides.

To further study the charge-discharge capacity and stability of batteries at different rates, we performed rate performance tests. Figure 4e showed the discharge specific capacity of HCF, TIT, and TIT/Fe$_3$C-CNT assembled into batteries at discharge rates of 0.2, 0.5, 1, 2, and 5 C, respectively. The discharge specific capacity of TIT/Fe$_3$C-CNT at different current densities was 1222, 926, 780, 694, and 580 mAh g^{-1}. When the current density dropped to 0.2 C, the discharge specific capacity increased to 977 mAh g^{-1}. When TIT was used as the sulfur host material for lithium-sulfur batteries, the discharge specific capacity under the same rates was 1040, 784, 647, 576, and 424 mAh g^{-1}, and when the current density dropped to 0.2 C, the discharge specific capacity increased to 768 mAh g^{-1}, all of these values were lower than the discharge specific capacity of TIT/Fe$_3$C-CNT as the sulfur host material. These results showed that TIT/Fe$_3$C-CNT exhibited better rate performance than TIT. The incorporation of Fe$_3$C and CNT enabled the battery to maintain a high specific capacity even under a high current

Batteries & Supercaps

Research Article
doi.org/10.1002/batt.202400224

Chemistry
Europe
European Chemical
Societies Publishing

density. In addition, the rate performance of HCF exhibited a lower discharge specific capacity compared to TIT/Fe$_3$C-CNT and TIT, further demonstrating the structure advantages of the designed TIT. Figure 4f showed the charge-discharge curves of HCF, TIT, and TIT/Fe$_3$C-CNT at a current density of 0.2 C. A comparison of the charge-discharge potential difference among the three samples reveals that TIT/Fe$_3$C-CNT exhibited a smaller potential difference than TIT and HCF. This suggests that the sample had lower electrochemical overpotential and electrode polarization, which was also consistent with the CV test results (Figure 4a). Figures 4(g–i) showed the charge-discharge curves of HCF, TIT, and TIT/Fe$_3$C-CNT at different rates, demonstrating that the three samples exhibited typical charge-discharge profiles of lithium-sulfur batteries at low current densities. TIT/Fe$_3$C-CNT exhibited the highest discharge capacity at the first plateau (2.3 V), suggesting that TIT/Fe$_3$C-CNT could offer ample space for accommodating the active material sulfur within its structure. The discharge specific capacity at the second platform (2.1 V) varied significantly among the three samples. With the increase in current density, both HCF and TIT experienced severe electrochemical polarization due to the shuttle effect caused by soluble lithium polysulfides in the charge-discharge process. The presence of Fe$_3$C in TIT/Fe$_3$C-CNT not only adsorbed lithium polysulfides dissolved in the electrolyte but also facilitated the conversion of long-chain lithium polysulfides to short-chain lithium polysulfides. Moreover, the three-dimensional CNT network exhibited a greater specific surface area, leading to enhanced contact between the sample and lithium polysulfides. This increased contact area improves material conductivity, accelerates the redox reaction of lithium polysulfides, and enhances the ability of the TIT/Fe$_3$C-CNT sample to mitigate the shuttle effect in lithium-sulfur batteries.

Figure 5a showed the curves of HCF, TIT, and TIT/Fe$_3$C-CNT at a current density of 0.5 C after 200 cycles. After 200 cycles, the specific capacity remained at 841 mAh g^{-1}, with a decay rate of 0.056% per cycle. In comparison, TIT and HCF only had discharges of 732 and 563 mAh g^{-1}, respectively, after 200 cycles at the same current density. Moreover, after subjecting TIT and TIT/Fe$_3$C-CNT to 400 cycles at a current density of 2 C and an active substance area loading of 2 mg cm^{-2}, the specific capacity of TIT/Fe$_3$C-CNT was measured at 660 mAh g^{-1}. In contrast, the specific capacity of TIT exhibited a significant decline after 200 cycles, reaching only 352 mAh g^{-1} after 300 cycles, as illustrated in Figure 5b. The TIT/Fe$_3$C-CNT sample exhibited significantly improved cycling performance at high current densities. This enhancement can be attributed to the dual functionality of the Fe$_3$C particles, based on their capacity to both adsorb and catalyze the conversion of lithium polysulfide. Additionally, the abundant conductive network of CNT enhances ion transport efficiency and accelerates the redox kinetics of the active material. While demonstrating high capacity and cycling stability at a low sulfur loading, the high sulfur loading is also important for high energy density in LSBs. To further investigate this, the cathode with a high sulfur loading of 4.5 mg cm^{-2} was synthesized. Figure S10 showed the charge and discharge curve tests at a current density of 0.1 C. It can be seen that the TIT/Fe$_3$C-CNT exhibited an initial discharge capacity of 1058 mAh g^{-1}, showcasing the consistently excellent performance of the TIT/Fe$_3$C-CNT, even under conditions of high sulfur load.

CV curves at different scan rates were tested for HCF, TIT, and TIT/Fe$_3$C-CNT, as shown in Figure 5(c–e). Peak currents (I_p) of Peaks A, B, and C were linearly fitted with the square root of the scan rate ($v^{0.5}$) based on the Randles-Sevcik equation (Equation 3–1). As shown in Figure 5f–h, the slopes of the three peaks for both HCF and TIT were lower than the slope for TIT/Fe$_3$C-CNT, indicating that TIT/Fe$_3$C-CNT had a higher lithium-ion migration rate.

$$I_p = 2.69 \times 10^5 n^{1.5} A D_{Li}^{0.5} + C_{Li} + v^{0.5} \qquad (3\text{–}1)$$

Finally, the batteries of HCF, TIT, and TIT/Fe$_3$C-CNT were disassembled after 100 cycles at a current density of 0.5 C, as illustrated in Figure 5(i–k). By comparing the separators of different batteries, it could be observed that both TIT (Figure 5j) and HCF (Figure 5k) had noticeable yellow stains on the separator surface, which were caused by the severe shuttle effect of lithium polysulfides during charge-discharge processes. In contrast, the separator surface of TIT/Fe$_3$C-CNT (Figure 5i) showed no noticeable traces of HCF, indicating that the presence of Fe$_3$C effectively adsorbed lithium polysulfides and mitigated the shuttle effect in the battery. Significant black precipitates identified as Li$_2$S was observed on the surfaces of TIT (Figure 5m) and HCF samples (Figure 5n), indicating the occurrence of severe shuttle effect in the two cases. In comparison, the surface of the TIT/Fe$_3$C-CNT lithium electrode (Figure 5l) had almost no black precipitates, demonstrating that the TIT/Fe$_3$C-CNT host material could mitigate the occurrence of the shuttle effect.

Conclusions

In a word, carbon composite materials with a tube-in-tube structure decorated by CNT and Fe$_3$C nanoparticles (TIT/Fe$_3$C-CNT) are designed in this work to have the following advantages as a sulfur host in lithium-sulfur batteries: (1) The tube-in-tube structure of carbon fiber provides a larger space for storing active sulfur, ensuring sufficient contact area between the electrode and the electrolyte; (2) The presence of Fe$_3$C facilitates the adsorption of soluble lithium polysulfides and promotes the catalytic conversion of sulfur species; (3) The Fe$_3$C particles catalytically generate a large number of CNT within the cavity of the sheath through the chemical vapor deposition process, and the three-dimensional network formed by the CNT is beneficial for shortening the diffusion path of electrons and lithium ions, and increasing the conductivity of the sample. Thanks to the above advantages, the multifunctional TIT/Fe$_3$C-CNT assembled battery demonstrated outstanding electrochemical rate performance and long-cycle stability. After 200 cycles at a current density of 0.5 C, the specific capacity of TIT/Fe$_3$C-CNT remained at 841 mAh g^{-1}, and the attenuation rate per cycle was only 0.056%. Additionally, TIT/Fe$_3$C-CNT exhibited a high specific capacity of 660 mAh g^{-1} after

Batteries & Supercaps

Research Article
doi.org/10.1002/batt.202400224

**Chemistry
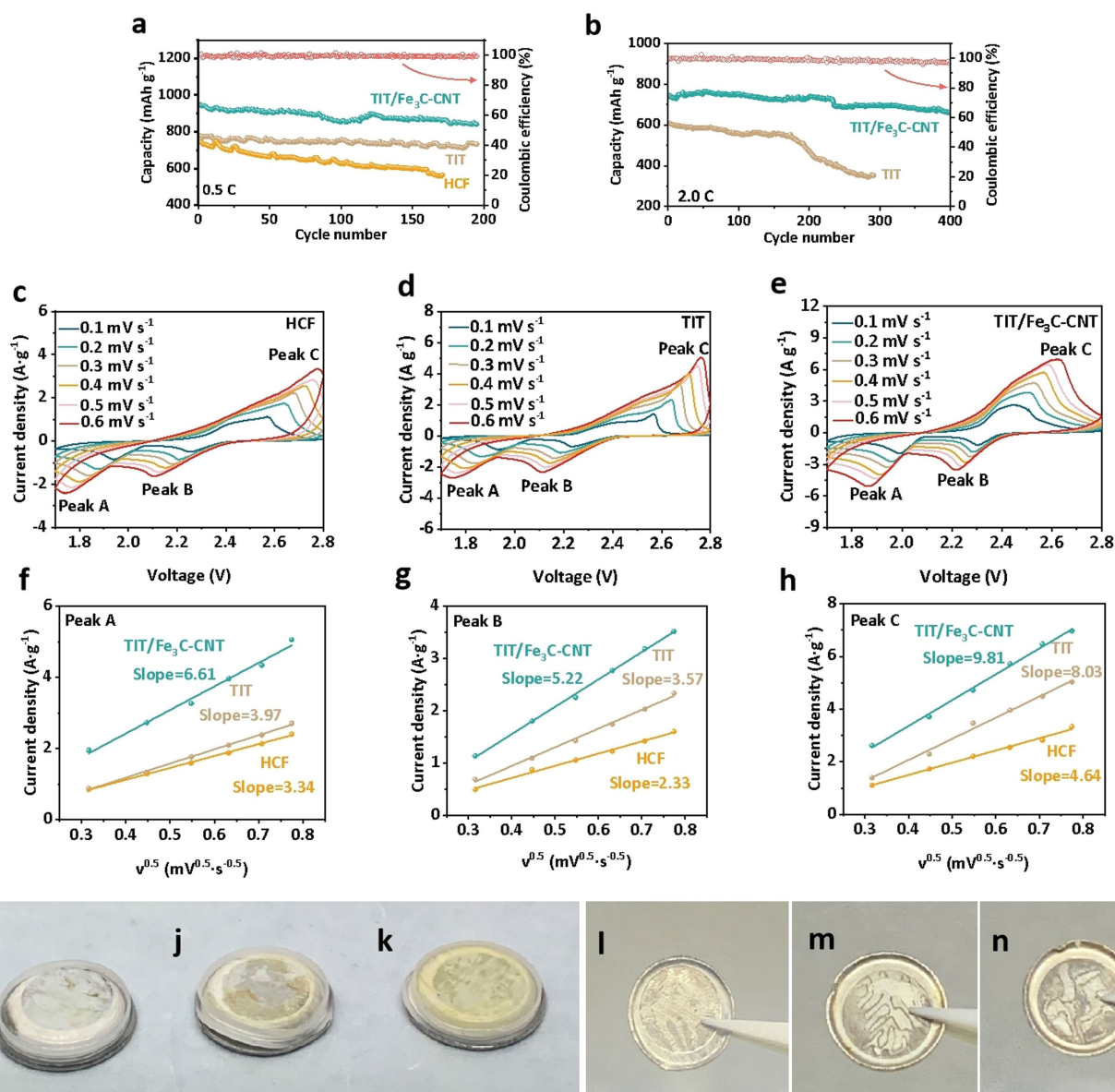Europe**
European Chemical
Societies Publishing

Figure 5. Cycle performance of HCF, TIT, and TIT/Fe₃C-CNT at 0.5 C (a) and 2 C (b). (c–e) CV curves of HCF, TIT, and TIT/Fe₃C-CNT at different rates. (f–h) Linear fit curves of the square root of peak current and sweep speed at Peak A, Peak B, and Peak C, respectively. (i–k) Optical photographs of TIT/Fe₃C-CNT, TIT, and HCF septa after 100 cycles at 0.5 C. (l–n) Optical photographs of the lithium wafer surfaces of TIT/Fe₃C-CNT, TIT, and HCF after 100 cycles at 0.5 C.

400 cycles, which was much higher than that of the TIT material under the same conditions.

The host material prepared in this paper needs to be ground and made into slurry after the sulfur load at high temperature, and finally coated on the surface of aluminum foil. The process may destroy the microstructure of the material and make the one-dimensional material fracture in the grinding process. In addition, the electrode collector fluid prepared by coating method is mostly aluminum foil, and the introduction of aluminum foil will undoubtedly increase the overall quality of the electrode, which is not conducive to improve the mass energy density of the battery. Studies have shown that the electrode materials with self-supporting function can not only effectively reduce the overall quality of the electrode to increase their energy density but can also simplify the sulfur

loading process, making the battery preparation easier.[40] In addition, most of the host materials with self-support properties are very flexible, which not only alleviates the volume expansion of lithium-sulfur batteries,[41] but also creates the possibility for the preparation of flexible batteries. Therefore, the host material can be electrospun to make self-support material and then load sulfur.

Experimental Section

Raw Materials

Polystyrene ($M_W = 350,000$) provided by Sigma-Aldrich Co., Ltd and polyvinylpyrrolidone ($M_W = 44,000–54,000$) supplied by Sinopharm

Batteries & Supercaps

Research Article
doi.org/10.1002/batt.202400224

Chemistry Europe
European Chemical
Societies Publishing

Chemical Reagent Co., Ltd. were employed for electrospinning. Pyrrole (99%) was obtained from Tokyo Chemical Industry Co., Ltd. N,N-Dimethylformamide and anhydrous ferric chloride were purchased from Sinopharm Chemical Reagent Co., Ltd. All chemicals are analytical grade and can be used without further purification.

Synthesis of HPS Fibers

PS and PVP particles were separately dissolved in dimethylformamide (DMF) to prepare PS (20 wt.%) and PVP (35 wt.%) spinning solutions, respectively. Subsequently, the PS solution was used as the shell solution and the PVP solution was used as the core solution for coaxial spinning at a working voltage of 15 kV, with spinning rates set at 160 and 20 $\mu L\,min^{-1}$ for the shell and core, respectively. The prepared PVP@PS fiber membrane was washed multiple times in water to obtain HPS, and solid PS fibers as a control.

Synthesis of HPS@FeCl$_3$-PPy Fibers

A certain amount of HPS was placed in a beaker containing concentrated sulfuric acid and stirred for 3 hours until the solution turned into a viscous state. The sulfonated HPS was obtained by diluting and filtering the viscous liquid, then thoroughly washing it with deionized water until a pH of neutral was reached. 1 g of sulfonated HPS was taken and added to 70 mL of deionized water with vigorously stirring. 0.1934 g of pyrrole monomer was dissolved in 10 mL of anhydrous ethanol, and the mixture was poured into the deionized water containing HPS. The solution was stirred for 3 hours under an argon atmosphere. Then, 1.075 g of FeCl$_3$ was dissolved in 20 mL of deionized water and added to the mixture. To produce PPy-coated hollow PS (HPS@PPy) without FeCl$_3$, some of the stirred black mixture was finally cleaned and filtered using deionized water, and the remaining black substance was filtered straight to produce HPS@FeCl$_3$-PPy.

Synthesis of TIT/Fe$_3$C-CNT Fibers

The obtained HPS@PPy fibers were placed in a tube furnace and carbonized under Ar atmosphere at a temperature of 800 °C for 2 hours, with a heating rate of 5 °C min^{-1}. After the sample was cooled to room temperature, the carbonized sample tube was collected as TIT (carbonized HPS@PPy spinning membrane). As reference samples, HCF (hollow carbonized fibers) were created by subjecting the ppy-coated solid PS fibers (PS@PPy) to the same carbonization process. The third group, HPS@FeCl$_3$-PPy, which contained FeCl$_3$, was subjected to the chemical vapor deposition technique of carbonization and catalytic preparation of CNT. The experimental procedure was as following: a tube furnace was used to carbonize 100 mg of dried HPS@FeCl$_3$-PPy and 2 g of dicyandiamide in a nitrogen atmosphere. After raising the temperature to 550 °C at a rate of 5 °C min^{-1}, it was kept for 20 minutes to ensure dicyandiamide react with FeCl$_3$ to generate Fe$_3$C and stimulate the formation of CNT.

Materials Characterization

The samples' morphology was analyzed through scanning electron microscopy (SEM, Apreo S HiVac) and transmission electron microscopy (TEM, JEM-2100 UHRS). X-ray diffraction (XRD) patterns were acquired using a Netherlands PANalytical X'pert PRO instrument with Cu–Kα radiation at 0.154 nm. X-ray photoelectron spectra (XPS) were measured utilizing the Thermo ESCALAB 250XI. Thermal characteristics were determined via thermogravimetric-differential thermal analysis (TG-DTA) employing a Thermogravimetric Analyzer (TG 209 F3 Tarsus) under a nitrogen atmosphere at a heating rate of 10 °C min^{-1}. Fourier-transform infrared spectroscopy (FTIR) was conducted using the Thermo Scientific Nicolet 6700. Raman spectra were obtained with the Labram HR Evolution system. The Brunauer–Emmett–Teller (BET) analysis and nitrogen adsorption–desorption isotherms were studied on the ASAP 2460 apparatus. Lastly, the electrolyte permeability was evaluated using a contact goniometer (OCS15EC, Germany).

Electrochemical Testing

In this study, the methodology adopted for sulfur loading is outlined as follows: The as-prepared host material was initially blended with a precise mass proportion of sublimed sulfur and thoroughly homogenized. Subsequently, the amalgamated mixture was encapsulated within a glove box, ensuring an inert gas-filled environment. Loading of sulfur was achieved by heating the sulfur-host composite in argon at 155 °C for a duration of 12 hours. Following this, a mixture comprising 70%–90% sulfur-carbon composite material and 10% polyvinylidene (PVDF) in N-methyl pyrrolidone (NMP) was stirred at 40 °C for 12 hours post cooling to ambient temperature. The resultant slurry was spread onto aluminum foil and dried overnight at 60 °C.

For the construction of lithium-sulfur batteries (LSBs), Li foil was employed as the anode, with coin cells (CR2025) assembled within an argon-filled glove box. A specific volume of 1.0 M LiTFSI was applied to both sides of the separator. The electrolyte formulation encompassed a solvent blend of 1,2-dimethoxyethane (DME) and 1,3-dioxane (DOL) in a 1:1 ratio by volume, augmented with a 2.0 wt% LiNO$_3$ additive. Coin cells underwent testing within a voltage range of 1.7–2.8 V. Electrochemical investigations of LSBs were conducted through cyclic voltammetry (CV) at a scanning rate of 0.1–0.6 mV s^{-1} and electrochemical impedance spectroscopy (EIS) measurements spanning frequencies from 0.01 to 100 kHz using an electrochemical workstation (CHI 660E).

Conflict of Interests

The authors declare no conflict of interest.

Data Availability Statement

The data that support the findings of this study are available from the corresponding author upon reasonable request.

Batteries & Supercaps

Research Article
doi.org/10.1002/batt.202400224

Chemistry
Europe
European Chemical
Societies Publishing

[1] F. Wu, V. Srot, S. Chen, M. Zhang, P. A. van Aken, Y. Wang, J. Maier, Y. Yu, *ACS Nano.* **2021**, *15*, 1509–1518.

[2] K. Li, G. Yuan, X. Liu, Q. Xie, L. Dong, Z. Li, H. Zhang, Z. Xie, S. Zhang, W. Lei, *Energy Storage Mater.* **2024**, *65*, 103194.

[3] Z. Zhu, T. Jiang, M. Ali, Y. Meng, Y. Jin, Y. Cui, W. Chen, *Chem. Rev.* **2022**, *122*, 16610–16751.

[4] G. May, A. Davidson, B. Monahov, *J. Energy Storage* **2018**, *15*, 145–157.

[5] W. Zhou, M. Chen, D. Zhao, C. Zhu, N. Wang, W. Lei, Y. Guo, L. Li, *Adv. Funct. Mater.* **2024**, 2402114.

[6] N. Yuan, Y. Deng, S. Wang, L. Gao, J. Yang, N. Zou, B. Liu, J. Zhang, R. Liu, L. Zhang, *Tungsten.* **2022**, *4*, 269–283.

[7] Y. Li, Q. Cai, L. Wang, Q. Li, X. Peng, B. Gao, K. Huo, P. Chu, *ACS Appl. Mater. Interfaces* **2016**, *36*, 23784–23792.

[8] X. Zhang, Y. Fan, M. Khan, H. Zhao, D. Ye, J. Wang, B. Yue, J. Fang, L. Zhang, J. Zhang, *Batteries & Supercaps* **2019**, *3*,1.

[9] D. Guo, M. Yuan, M. Zheng, M. Li, C. Nan, G. Sun, X. Huang, H. Li, *J. Energy Chem.* **2022**, *73*, 5–12.

[10] J. Luo, X. Liu, W. Lei, Q. Jia, S. Zhang, H. Zhang, *Adv. Fiber Mater.* **2022**, *4*, 1656–1668.

[11] S.-H. Chung, A. Manthiram, *Adv. Mater.* **2019**, *31*, 1901125.

[12] M. Zhao, B. Li, X. Zhang, J. Huang, Q. Zhang, *ACS Cent. Sci.* **2020**, *6*, 1095–1104.

[13] S. Li, W. Zhang, J. Zheng, M. Lv, H. Song, L. Du, *Adv. Energy Mater.* **2021**, *11*, 2000779.

[14] J. Xie, Y.-W. Song, B.-Q. Li, H.-J. Peng, J.-Q. Huang, Q. Zhang, *Angew. Chem. Int. Ed.* **2020**, *59*, 22150–22155.

[15] T. Wang, J. He, Z. Zhu, X.-B. Cheng, J. Zhu, B. Lu, Y. Wu, *Adv. Mater.* **2023**, *35*, 2303520.

[16] G. Di Donato, T. Ates, H. Adenusi, A. Varzi, M. Navarra, S. Assunta Passerini, *Batteries & Supercaps* **2022**, *5*, e202200097.

[17] X. Zhu, L. Wang, Z. Bai, J. Lu, T. Wu, *Nano-Micro Lett.* **2023**, *15*, 75.

[18] F. Pei, A. Fu, W. Ye, J. Peng, X. Fang, M.-S. Wang, N. Zheng, *ACS Nano.* **2019**, *13*, 8337–8346.

[19] X. Li, B. Gao, X. Huang, Z. Guo, Q. Li, X. Zhang, P. Chu, K. Huo, *ACS Appl. Mater. Interfaces.* **2019**, *11*, 2961–2969.

[20] Y. Xiang, L. Lu, A. Kottapalli, Y. Pei, *Carbon Energy.* **2022**, *4*, 346–398.

[21] J. Luo, K. Guan, W. Lei, S. Zhang, Q. Jia, H. Zhang, *J. Mater. Sci. Technol.* **2022**, *122*, 101–120.

[22] A. Raulo, G. Jalilvand, *Nano Energy.* **2024**, *122*, 109265.

[23] A. Abdul Razzaq, Y. Yao, R. Shah, P. Qi, L. Miao, M. Chen, X. Zhao, Y. Peng, Z. Deng, *Energy Storage Mater.* **2019**, *16*, 194–202.

[24] Z. Li, C. Qi, Q. Chang, J. Jin, Y. Lu, Z. Wen, *Compos Part B-Eng.* **2023**, *257*, 110679.

[25] Q. Yang, N. Deng, Y. Zhao, L. Gao, B. Cheng, W. Kang, *Chem. Eng. J.* **2023**, *451*, 138532.

[26] K. Guan, Y. Yu, H. Liu, J. Luo, W. Lei, H. Zhang, *Appl. Surf. Sci.* **2023**, *638*, 157963.

[27] P. Ding, T. Yan, K. Li, Q. Wu, X. Zhu, H. Chen, A. Ju, *J. Alloys Compd.* **2022**, *928*, 167056.

[28] H. Li, W. Yang, N. Wu, L. Sun, P. Shen, X. Wang, Y. Li, *Appl. Surf. Sci.* **2023**, *617*, 156485.

[29] G. Mumbach, A. Bolzan, R. Machado, *Polymer.* **2020**, *209*, 122940.

[30] Y. Yang, C. Wang, C. Tian, H. Guo, Y. Shen, M. Zhu, *J Mate Chem B.* **2018**, *6*, 6848–6857.

[31] Y.-S. Liu, C. Ma, Y.-L. Bai, X.-Y. Wu, Q.-C. Zhu, X. Liu, X.-H. Liang, X. Wei, K.-X. Wang, J.-S. Chen, *J. Mater. Chem. A* **2018**, *6*, 17473–17480.

[32] C. Zhou, X. Li, H. Jiang, Y. Ding, G. He, J. Guo, Z. Chu, G. Yu, *Adv. Funct. Mater.* **2021**, *31*, 2011249.

[33] J. Lim, X. Jin, S. Hwang, C. Scheu, *Adv. Funct. Mater.* **2020**, *30*, 36.

[34] J.-Q. Huang, B. Zhang, Z.-L. Xu, S. Abouali, M. Akbari Garakani, J. Huang, J.-K. Kim, *J. Power Sources* **2015**, *285*, 43–50.

[35] J. Wang, Z. Zhang, X. Yan, S. Zhang, Z. Wu, Z. Zhuang, W. Han, *Nano-Micro Lett.* **2019**, *12*, 4.

[36] T. Zhu, Y. Sha, H. Zhang, Y. Huang, X. Gao, M. Ling, Z. Lin, *ACS Appl. Mater. Interfaces* **2021**, *13*, 20153–20161.

[37] W. Yang, X. Liu, X. Yue, J. Jia, S. Guo, *J. Am. Chem. Soc.* **2015**, *137*, 1436–1439.

[38] Y.-Z. Chen, C. Wang, Z.-Y. Wu, Y. Xiong, Q. Xu, S.-H. Yu, H.-L. Jiang, *Adv. Mater.* **2015**, *27*, 5010–5016.

[39] J. Zheng, G. Guo, H. Li, L. Wang, B. Wang, H. Yu, Y. Yan, D. Yang, A. Dong, *ACS Energy Lett.* **2017**, *2*, 1105–1114.

[40] W. Wang, H. Li, C. Ding, Z. Guo, G. Wang, *J. Energy Storage* **2023**, *71*, 108072.

[41] J. Ao, Y. Xie, Y. Lai, M. Yang, J. Xu, F. Wu, S. Cheng, X. Wang, *Sci. China Mater.* **2023**, *66*, 8.